THE JOURNAL OF PHYSICAL CHEMISTRY A

Article

Cite This: J. Phys. Chem. A 2019, 123, 10047−10056

pubs.acs.org/JPCA

In Situ Formed Ir_3Li Nanoparticles as Active Cathode Material in Li−Oxygen Batteries

Published as part of The Journal of Physical Chemistry virtual special issue "Leo Radom Festschrift".

Avik Halder,[†] Anh T. Ngo,[†] Xiangyi Luo,[‡] Hsien-Hau Wang,[†] J. G. Wen,[§] Pedram Abbasi,[∥] Mohammad Asadi,[∥] Chengji Zhang,[†,⊥] Dean Miller,[§] Dongzhou Zhang,[#] Jun Lu,[‡] Paul C. Redfern,[†] Kah Chun Lau,[¶] Rachid Amine,[†,▽] Rajeev S. Assary,[†] Yun Jung Lee,[○] Amin Salehi-Khojin,[∥] Stefan Vajda,*[,†,◆,^] Khalil Amine,*[,‡,□,⬡] and Larry A. Curtiss*[,†]

[†]Materials Science Division, Argonne National Laboratory, Argonne, Illinois 60439, United States

[‡]Chemical Sciences and Engineering Division, Argonne National Laboratory, Argonne, Illinois 60439, United States

[§]Center for Nanoscale Materials, Argonne National Laboratory, Argonne, Illinois 60439, United States

[∥]Department of Mechanical and Industrial, University of Illinois at Chicago, Chicago, Illinois 60607, United States

[⊥]Department of Civil and Materials Engineering, University of Illinois at Chicago, Chicago, Illinois 60607, United States

[#]Partnership for Extreme Crystallography, Argonne National Laboratory, Argonne, Illinois 60439, United States

[¶]Department of Physics and Astronomy, California State University, Northridge, California 91330, United States

[▽]Department of Chemical Engineering, University of Illinois at Chicago, Chicago, Illinois 60607, United States

[○]Department of Engineering, Hanyang University, Seoul 133-791, Republic of Korea

[◆]Institute for Molecular Engineering, The University of Chicago, Chicago, Illinois 60637, United States

[^]Department of Nanocatalysis, J. Heyrovský Institute of Physical Chemistry, Czech Academy of Sciences, Dolejškova 3, 18223 Prague 8, Czech Republic

[□]Department of Material Science and Engineering, Stanford University, 450 Serra Mall, Stanford, California 94305, United States

[⬡]Institute for Research and Medical Consultations (IRMC), Imam Abdulrahman Bin Faisal University (IAU), Dammam 34212, Saudi Arabia

Supporting Information

ABSTRACT: Lithium−oxygen ($Li-O_2$) batteries are a promising class of rechargeable Li batteries with a potentially very high achievable energy density. One of the major challenges for $Li-O_2$ batteries is the high charge overpotential, which results in a low energy efficiency. In this work size-selected subnanometer Ir clusters are used to investigate cathode materials that can help control lithium superoxide formation during discharge, which has good electronic conductivity needed for low charge potentials. It is found that Ir particles can lead to lithium superoxide formation as the discharge product with Ir particle sizes of ∼1.5 nm giving the lowest charge potentials. During discharge these 1.5 nm Ir nanoparticles surprisingly evolve to larger ones while incorporating Li to form core−shell structures with Ir_3Li shells, which probably act as templates for growth of lithium superoxide during discharge. Various characterization techniques including DEMS, Raman, titration, and HRTEM are used to characterize the LiO_2 discharge product and the evolution of the Ir nanoparticles. Density functional calculations are used to provide insight into the mechanism for formation of the core−shell Ir_3Li particles. The *in situ* formed Ir_3Li core−shell nanoparticles discovered here provide a new direction for active cathode materials that can reduce charge overpotentials in $Li-O_2$ batteries.

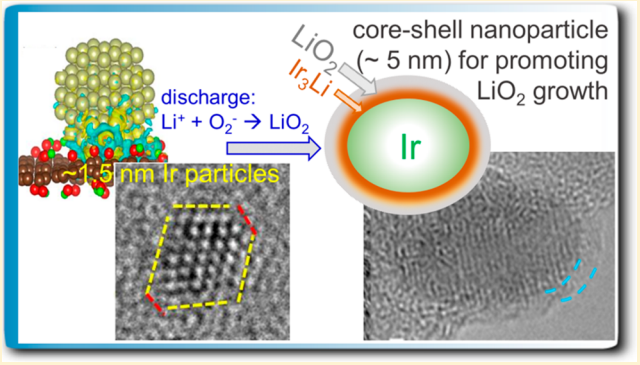

1. INTRODUCTION

The use of lithium−oxygen bonds for storage of electrical energy is of much interest because of the possibility for

Received: July 18, 2019
Revised: September 25, 2019
Published: October 28, 2019

DOI: 10.1021/acs.jpca.9b06875
J. Phys. Chem. A 2019, 123, 10047−10056

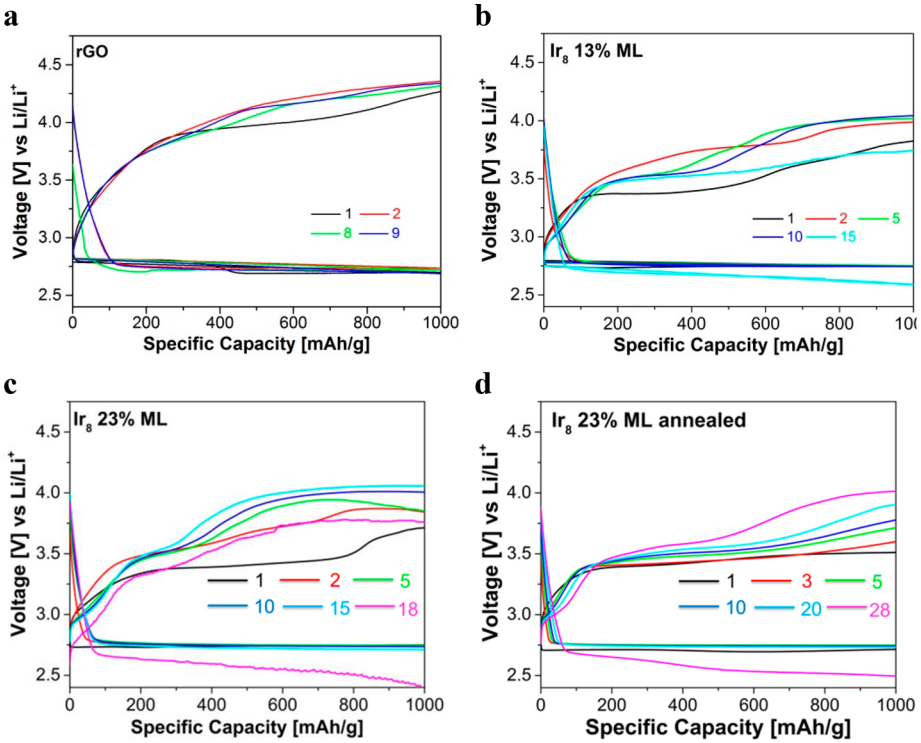

Figure 1. Voltage profiles for rGO and Ir_8 clusters on rGO: (a) pristine rGO, (b) 13% ML Ir_8–rGO, (c) 23% ML Ir_8–rGO, and (d) annealed 23% ML Ir_8–rGO. Ir_8 cluster loading is given as a fraction of a monolayer (ML). The cell is operated with discharge limited to 1000 mAh g^{-1} capacity at a current density of 100 mAg^{-1}.

achieving very high energy densities needed for long-range electric vehicles.[1−5] The development of batteries based on formation and decomposition of covalent lithium−oxygen bond requires fundamental understanding of Li−O_2 electrochemistry whereby lithium peroxide (Li_2O_2) is usually formed during discharge and decomposed during charge. In some cases, it has been found that the reaction product formed during discharge can be a mixture of components such as lithium superoxide (LiO_2) and lithium hydroxide (LiOH) along with Li_2O_2 with the exact composition depending on the experimental conditions.[6−8] It has also been reported that LiO_2 can be stabilized in a Li−O_2 electrochemical cell by using a suitable cathode material[9] and it had a low charge potential probably because of the good electronic conductivity of LiO_2, which is a half metal.

Lithium superoxide is thermodynamically unstable with respect to Li_2O_2 and O_2[10] and therefore is difficult to stabilize and study. In the case of the Li−O_2 battery[9] where LiO_2 was observed, it was speculated that a novel templating growth mechanism involving Ir_3Li intermetallic particles was responsible for stabilizing crystalline LiO_2. However, the study only reported evidence of the presence of some Ir_3Li crystal structures on the cathode after the battery was run. The cathode used in the cell was based on Ir nanoparticles of sizes ranging from a couple of atoms to large agglomerates on a reduced graphene oxide (rGO) support, so it was not clear what size particle was responsible for LiO_2 formation or which ones were transformed to the Ir_3Li intermetallic.

In the work presented here, we have used size-specific subnanometer Ir clusters on a rGO support to probe the evolution of Ir particles in a Li−O_2 cell and the role of this evolution in stabilizing of LiO_2, which can be important for reducing charge potentials in Li−O_2 batteries. The size-specific clusters have the advantage of being able to help elucidate the role that particle size plays in the discharge and charge mechanisms, such as we have reported previously for how size-specific Ag clusters affect the discharge product morphology.[11] In the work on the Ag clusters, even clusters as small as three atoms were found to be active in a Li−O_2 battery. The objective of the current work based on size-specific Ir clusters was 2-fold. The first was to determine what role Ir particle size plays in lithium superoxide stabilization in a Li−O_2 battery, i.e., whether LiO_2 is more likely to form with a certain Ir particle size. The second was to obtain insight into both the role of the Ir_3Li intermetallic and how it forms. The latter is of much interest since previously Ir_3Li had only been synthesized at very high temperatures[12] whereas Ir_3Li was formed in a Li−O_2 battery run at room temperature. In section 2 the experimental and theoretical methods used in this study are presented. In section 3 the results of the Li−O_2 batteries run with different size Ir particles are presented as well as characterization results. In section 4 the discharge mechanism is discussed.

2. METHODS

2a. Ir_n–rGO Cathode Material Preparation. Graphene oxide (GO) for the cathode was prepared by following a modified Hummers method.[13,14] Reduced graphene oxide (rGO) was prepared by treating GO with $NaBH_4$ in ethylene glycol as reported previously.[9] After synthesis, the rGO powders were dried at 80 °C under vacuum for 24 h. The oxygen cathode was prepared by mixing rGO powders with polyvinylidene difluoride (PVDF) in *N*-methyl-2-pyrrolidone (NMP) solution with a weight ratio of 8:2. The resulting slurry was coated on a gas-diffusion layer (Sigracet GDL 35 BC, SGL carbon) and dried for 12 h at 100 °C under vacuum to remove the residual solvent.

DOI: 10.1021/acs.jpca.9b06875
J. Phys. Chem. A 2019, 123, 10047−10056

Ligand-free subnanometer Ir_n clusters of a specific size were then deposited on the reduced graphene oxide (rGO) using the same technique as for previously reported for Ag_n clusters on a carbon substrate.[11] The rGO surface is covered by a fraction of a monolayer with size-selected Ir_n clusters of sizes 2, 4, and 8 atoms for this study. The clusters were generated in a high vacuum cluster apparatus in a molecular beam, then size-selected with atomic precision and subsequently soft landed on the support material[15] (see Figure S1 for schematic of the cluster deposition apparatus, and Figure S2 for a typical mass spectrum of Ir clusters). The total amount of deposited Ir clusters were a few tens of nanograms (~10 ng loading necessary for every 10% of an atomic monolayer (ML) equivalent coverage). The clusters are bare, thus free of any ligand effects. The size and crystallinity of the deposited nanoclusters were further tuned by annealing of the samples under vacuum.

2b. Voltage Profiling and Electrochemical Tests. A Swagelok-type cell was used to perform the electrochemical testing.[16] The assembly was placed inside a home-built glass chamber, which was filled with ultrahigh purity O_2 at 1 bar pressure to avoid any negative effects of N_2, humidity, and CO_2. The cell was composed of a Li metal anode, 1 M $LiCF_3SO_3$ in tetraethylene glycol dimethyl ether (TEGDME) impregnated into a glass fiber separator as electrolyte, and a porous Ir_n−rGO cathode with the diameter of 7/16 in. The porous cathode was exposed to the O_2 atmosphere inside the glass chamber through an Al grid. The voltage profiles shown in Figure 1 were attained using a MACCOR cycler. The charge−discharge cycle was performed over a 10 h time-control mode at a constant current density of 100 mA g^{-1} within the voltage range 2.2−4.5 V.

2c. Characterization Techniques for Cathode and Discharge Products. Spherical and chromatic aberration corrected high resolution transmission electron microscopy (HRTEM, FEI Titan 80-300) and scanning transmission electron microscopy (STEM, FEI Talos) operated at 80 keV were used for imaging the Ir_n−rGO cathode before and after the electrochemical testing to collect information about the evolution in the cathode nanostructures and particle size distribution. For imaging the Ir particles, the rGO coating on the TEM grids was obtained by a drop casting technique. The rGO powder was scraped from the cathode surface to ≈5 mL dimethyl ether in a container, which was then ultrasonically dispersed for 5 min to prepare a dilute solution. The suspension was subsequently dripped on to the copper grid and dried. The grids with the rGO layer on it were then attached to a SiO_2 chip using carbon based paint (LEIT-C Conductive Carbon Cement) and placed inside the cluster deposition machine to deposit the Ir clusters directly on the top of it. The cluster coverage on the TEM grids was kept the same as that used for the Ir_n−rGO cathodes. For imaging the discharged sample, the top surface of the Ir_n−rGO cathodes was directly scraped onto the TEM grid and then a drop of ethanol was used to disperse the powder uniformly on the grid. Both HRTEM and STEM data were analyzed using the Digital Micrograph software and the statistical analysis was done using Matlab to deduce the particle distribution. In addition, the morphology of the discharge products was determined using field-emission scanning electron microscopy (SEM, Hitachi S-4700). The images were collected right after the electrochemical tests, and the SEM specimens were prepared under ultrahigh purity Argon inside a glovebox.

High energy X-ray diffraction (HEXRD) was performed to characterize the phase structures of the deposited Ir clusters on a rGO surface and the discharge products. The XRD on cluster samples before the electrochemical testing was performed at the beamline 13-BM of the Advanced Photon Source (APS) of Argonne National Laboratory using a wavelength of 0.434 Å (beam dimension: 12 × 18 μm). The discharged cathode was tested at Sector 11ID-C at a wavelength of 0.117418 Å (beam dimension: 0.5 × 0.5 mm). In order to avoid any side reactions from the air during the measurement, the samples were sealed with a protective film of Kapton tape inside the glovebox. HEXRD patterns were collected in transmission mode using a 2D detector. Dioptas and Fit2d software were used for data transformation by integrating the 2D patterns to deduce the intensity versus θ plot.

Raman spectra of the discharged cathode were obtained using a Renishaw inVia microscope spectrometer with a HeNe laser at exciting wavelength of 633 nm. The discharge cathode sample was loaded in a gastight Raman cell with a glass or quartz window inside a glovebox under ultrahigh purity Argon. A 50× ultralong working distance (ULWD) microscope lens was used. Raman spectrum collection was set up in a 180° reflective mode. The laser intensity applied was roughly 10% of the maximum 13 mW available. The signal averaging mode was employed and the collection time constant setting varied from 30 to ~100 s.

DEMS measurements were carried out in a cell composed of a gas diffusion layer (GDL) with 0.721 mg/cm^2 of Ir_8−rGO catalyst as the cathode, 0.5 mm stainless steel spacer, 0.25 mm thick lithium chip, a 0.26 mm thick glassy fiber separator, and 1 M LiTFSI/TEGDME electrolyte. This configuration provides the head space of ~115 μL in the cell. The current of 0.0721 mA was applied to the cell to achieve the 100 mAg^{-1} current density, consistent with other performed experiments in this work. Experimental setup consisted of a MTI potentiostat and a mass spectrometer (Hiden Analytical). To correlate the oxygen partial pressure variation in the differential electrochemical mass spectrometry (DEMS) and number of moles of oxygen in the cell head space, we calibrated the instrument with different concentrations of pure O_2 (99.99%, Praxair) in research grade argon (99.99%, Praxair) and injected the samples in the mass spectrometer.

2d. Computational Methods. All the density functional theory (DFT) calculations are carried out using the VASP code.[17,18] All the calculations were spin polarized and carried out using the gradient corrected exchange−correlation functional of Perdew, Burke, and Ernzerhof (PBE)[19] under the projector augmented wave (PAW) method with planewave basis sets up to kinetic energy cutoff of 400 eV within Γ point unless noted. In all cases, the valence electrons for Li, O, C, H, and Ir atoms are 2s, 2s 2p, 2s 2p, 1s, and 5d 6s, respectively, and the remaining electrons were kept frozen.

3. RESULTS

3a. Voltage Profiles of Li−O_2 Cells Using Various Size Ir Particles. A constant current density of 100 mA/g was applied for both the charge and discharge cycles. The cell was cycled within a capacity limit of 1000 mAh/g to avoid the parasitic reactions. The voltage profile of a pristine rGO cathode is shown in Figure 1a. It has a charge potential of ~4.2 V and discharge of ~2.7 V. Cathodes modified by adding Ir_n (n = 2, 4, 8) clusters on the rGO supports were then investigated. The voltage profiles with Ir_8−rGO cathodes with a surface

DOI: 10.1021/acs.jpca.9b06875
J. Phys. Chem. A 2019, 123, 10047−10056

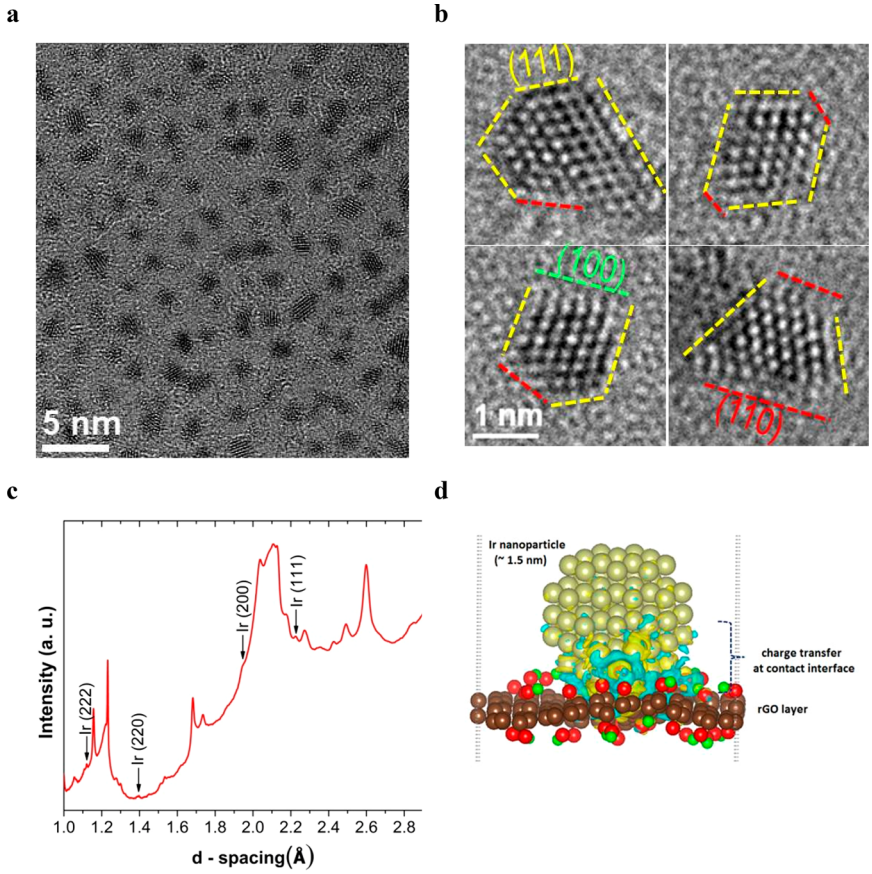

Figure 2. Characterization of annealed Ir_8−rGO cathode. (a) HRTEM image of 23% ML Ir_8−rGO cathode after annealing under vacuum for 24 h at 100 °C. (b) HRTEM image of annealed 23% ML Ir_8−rGO cathode showing crystalline facets of the Ir nanoparticles. (c) HEXRD of annealed 23% ML Ir_8−rGO cathode showing Ir crystalline peaks. The other large unmarked peaks are from the rGO. (d) DFT calculations for an Ir_{79} nanoparticle on rGO showing electron density changes at the Ir/rGO interface where the "yellow" regions represent an increase in electron density and "light blue" regions a decrease in electron density. Overall there is electron transfer to the nanoparticle.

coverage of 13% and 23% ML equivalent are shown in Figure 1b,c. The charging curve on the first cycle for 23% ML (Figure 1c) is mainly at ∼3.4 V with a second region between ∼800 and 1000 mAh/g that rises to ∼3.7 V. The second region may be due to the presence of a small amount of Li_2O_2 as we have found previously for an activated carbon cathode,[6,20] although in that case the second region was a more pronounced plateau at a higher voltage and could be accounted for by the presence of a large amount of Li_2O_2. The charging curve on the first cycle for 13% ML (Figure 1b) is at ∼3.4 V with a second region between ∼500 and 1000 mAh/g that rises to ∼3.7 V, which suggests somewhat more Li_2O_2 than for the higher 23% coverage. The 13% and 23% results (Figure 1b,c) are consistent with titration results given later showing the presence of some Li_2O_2 for the first cycle for these cathodes. On subsequent cycles the charge potentials for these two coverages increase with no really distinct regions as found for the first cycle probably due to changes to the Ir on cycling.

The 23% ML coverage with Ir_8 clusters was annealed under vacuum at 100 °C for 24 h to increase the size of the clusters and a significant lowering of the charge voltage profile was observed as shown in Figure 1d as the charge potential was ∼3.4 V on the first cycle with a small rise to ∼3.8 V after 20 cycles. We also investigated Ir clusters of two and four atoms and found charge potentials similar to the unannealed 13% ML Ir_8 clusters (Figure S3). The annealed Ir_8−rGO sample was chosen for detailed study in this work because of its low charge overpotential that was similar to that found the Ir−rGO cathode with Ir nanoparticles of sizes ranging from a couple of atoms to large agglomerates in our previous study.[9] Although the detailed study reported in this paper is on the annealed Ir clusters, it is noteworthy that the unannealed supported small Ir clusters (n = 2, 4, 8) are also very active in the Li−O_2 battery performance as shown in the voltage profiles in Figure 1 and Figure S3, consistent with what was found previously for small Ag clusters (n = 3, 9, 15).[11]

3b. Characterization of Annealed Ir_8 Clusters. The morphology and size of the unannealed and annealed Ir_8 clusters was investigated by HRTEM before discharge. The HRTEM images of the annealed Ir_8 clusters in Figure 2a,b show that they are aggregated into nanoparticles. In order to find an accurate estimate of the particle size distribution, we imaged the annealed Ir_8 particles using high angle annular dark-field (HAADF) in scanning transmission electron microscopy (STEM) mode, from which the mean size of the particles was found to be 1.5 nm (Figure S4) with most of the nanoparticles having crystalline facets. The Miller indices for the planes (111), (110), and (100) are identified in Figure 2b. The HEXRD of the annealed cathode material is shown in Figure 2c, where we identify the (111), (200), (220), and (222) peaks corresponding to crystalline Ir, in addition to large peaks from the rGO.

The images from HRTEM for the unannealed Ir_8 clusters on rGO are also shown in Figure S4. The unannealed Ir_8 clusters

DOI: 10.1021/acs.jpca.9b06875
J. Phys. Chem. A 2019, 123, 10047−10056

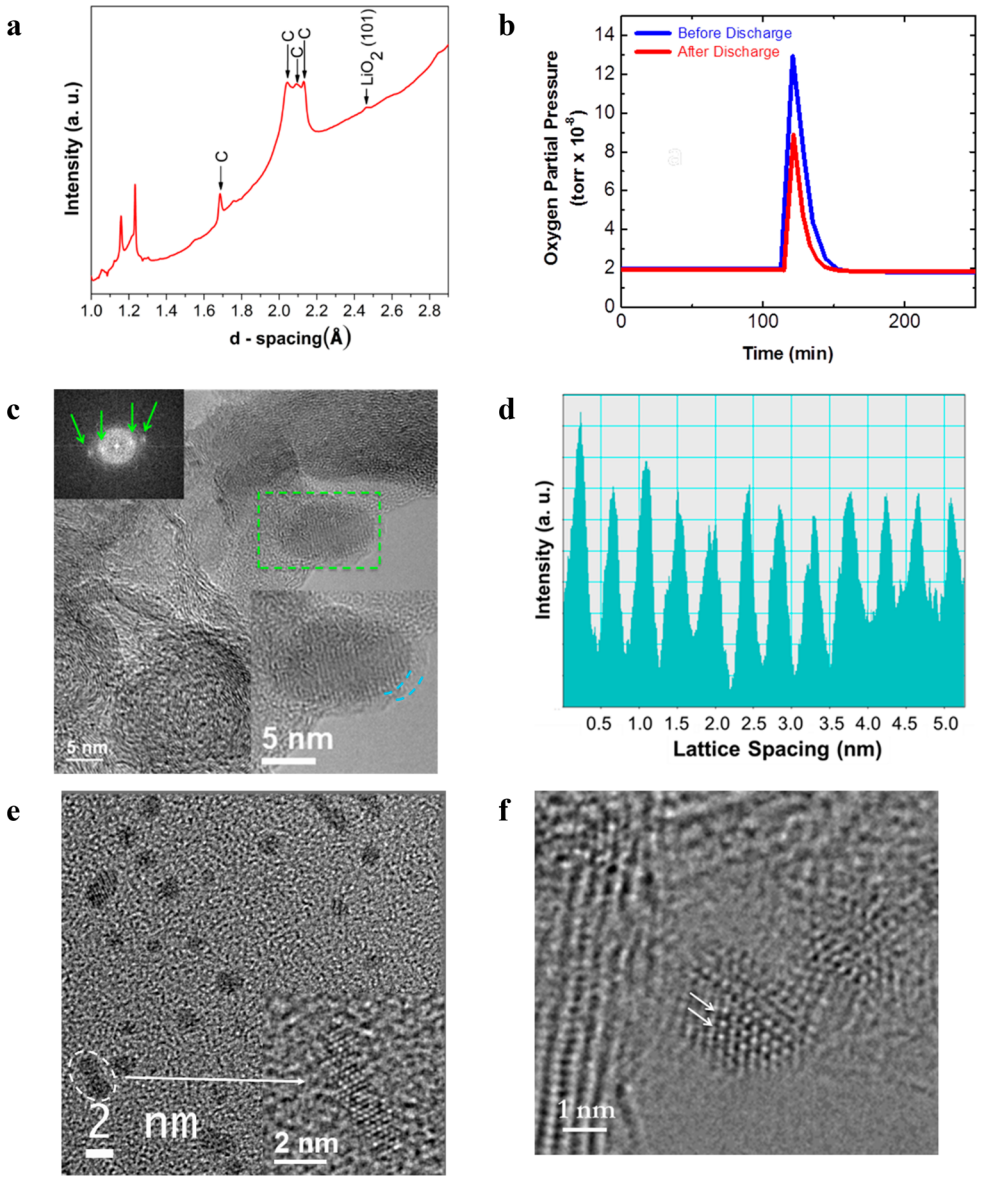

Figure 3. Characterization of annealed Ir_n−rGO cathode after discharge and charge by HRTEM imaging. (a) HEXRD image of discharged cathode. (b) DEMS result for first cycle discharge reaction with O_2 partial pressure measured before and after discharge reaction. (c) Individual ∼5 × 10 nm particle formed on the cathode after second discharge. The upper left inset shows a fast Fourier transform (FFT) on the nanoparticle surface with the diffraction peaks consistent with Ir_3Li; the lower right inset shows a close up of the nanoparticle with a thin layer of ∼1−2 nm marked by dashed cyan line on the surface of the nanoparticle, which may be due to the discharge product. (d) Lattice spacing of ∼4.1 Å for the nanoparticle in (c), which is identical with that of Ir_3Li. (e) TEM images of cathodes discharged only to 300 mAh/g. The inset shows two clusters getting together to form aggregate. (f) TEM image of the surface of a ∼5 nm particle after charging following first (full) discharge, showing the presence of Ir_3Li. The arrows mark the positions where Li has intercalated into the Ir nanoparticle surface. (c) is collected at FEI Talos, and (e) and (f) are collected at FEI Titan 80-300. Note also that the images are of scrapings from the cathode.

show evidence of agglomeration (mean size of 0.91 nm) at higher coverage (23% ML), but little at the lower coverage (13% ML). It has been previously pointed out that low coverage of supported small clusters is needed to prevent agglomeration even at room temperature, for example, for small silver clusters on graphitized carbon partially coated by alumina.[11]

Density functional theory (DFT) geometry relaxation of an Ir_{79} nanoparticle based on the bulk Ir structure on an rGO support is shown in Figure 2d. The DFT calculations indicate that the Ir_{79} nanoparticle has a dimension of ∼1.5 nm with an average Ir−Ir bond distance of 2.75 Å close to the Ir crystalline bulk of 2.72 Å after relaxation.[21] The nanoparticle has (111), (100), and (110) crystalline facets similar to that observed in some of the HRTEM images. The DFT calculations indicate that there is electron transfer from the rGO support to the Ir nanoparticle as shown in Figure 2d. This could facilitate oxygen reduction or evolution at the crystalline Ir sites of the cathode. A substantial electronic density of states (DOS), which showed a metallic-like feature, is found at the Fermi surface, E_F, and is largely from the Ir atoms in the Ir_{79}−rGO calculation (see Figure S5)

3c. Discharge Product Characterization. The discharge product on the annealed 23% ML Ir_8 cathode material taken after second discharge from the first cycle at a capacity of 1000 mAh/g was investigated using SEM, HEXRD, and HRTEM.

DOI: 10.1021/acs.jpca.9b06875
J. Phys. Chem. A 2019, 123, 10047−10056

The SEM result shown in Figure S6 does not give any indication of toroids or obvious 3-D nanoparticles on the surface as many previous studies have found.[5,6] The HEXRD spectrum in Figure 3a of the same sample also shows no peak due to Li_2O_2 or definite evidence for LiO_2 except one small (101) peak but does show carbon peaks from the rGO supports. The lack of any clear XRD evidence may be due to the formation of a thin film as opposed to toroids or nanoparticles, although the capacity is still reasonable at 1000 mAh/g. The different morphology (film-like) in this study compared to our previous study[9] (rod like) may be due to differing nucleation conditions such as the nucleation sites provided by the different Ir particle sizes in the two studies. This has been found before where size-selected Ag clusters of three sizes (3, 9, and 15 atoms) gives Li_2O_2 morphologies ranging from film-like to various sizes of toroids.[11]

The discharge product formed using the annealed 23% ML Ir_8−rGO cathode was further characterized by multiple techniques including DEMS, Raman, and titration. All are consistent with the formation of LiO_2 as the discharge product.

The DEMS experiment was performed by applying a current density of 100 mA/g and detecting the partial pressure of O_2 under ultrahigh vacuum (10^{-8} Torr) before and after the first cycle discharge process for the annealed 23% ML Ir_8 cathode. The partial pressure variation of the O_2 before and after the discharge process shown in Figure 3b corresponds to the consumption of 2.56×10^{-6} mol of O_2 using the standard calibration curve plotted in Figure S7. This measurement results in a 1.05 e^-/O_2 ratio that is consistent with the formation of lithium superoxide as the product during the discharge process.

Raman spectra collected from the discharge product after the first cycle at 1000 mAh/g show a peak at ∼1125 cm^{-1} for the annealed 23% ML Ir_8 cathode (Figure S8). This peak has been associated with the O−O stretching in the lithium superoxide by various studies.[7,22] In some cases a peak at ∼1495 cm^{-1} associated with LiO_2−C[22,23] was observed (Figure S8). No peaks were observed for any side reaction products like Li_2CO_3. In addition, no Raman peaks are observed for Li_2O_2 species. The LiO_2 Raman peaks are weak probably due to the formation of a very thin superoxide film on the cathode surface as observed from the HRTEM and HAADF images presented later in the text. Raman spectra were also collected for samples from the first and second discharge and stored under Ar inert atmosphere for 10 days (see Figure S9). In addition to the peak at 1125 cm^{-1}, additional peaks at ∼1041 cm^{-1}, which are due to $LiRCO_3$ formation as a result of LiO_2 reacting with the electrolyte over a prolonged time were observed.[6,23] A more detailed account of LiO_2 Raman peaks including evidence that they are not from the PVDF binder[24] has been presented elsewhere.[25]

Titration was performed on the annealed 23% ML Ir_8 cathode material after the first discharge cycle. A $Ti^{IV}OSO_4$ based technique was used to determine the amount of Li_2O_2 present in the discharge product.[26] When the acidic Ti(IV)-OSO_4 solution was added to this Ir_8−rGO sample, no color change was observed for the solution and a very weak UV peak was obtained in the UV−vis spectra (Figure S10), indicating the absence of Li_2O_2 in the discharge product. Titration results (Figure S10) are also given for the unannealed 13% and 23% ML Ir_8 cathodes and are consistent with small amounts of Li_2O_2 being present, as indicated earlier in the discussion of the charge potentials.

3d. Characterization of the Ir Nanoparticles after Discharge. HRTEM and HAADF images were taken of the Ir nanoparticles from the annealed 23% ML Ir_8 cathode after the first discharge cycle. The HRTEM images are shown in Figure 3 (see Figure S11 for EDS spectrum of the imaging area). The images demonstrate that the Ir nanoparticles, which were in the size range 0.5−3 nm, have unexpectedly evolved during the discharge process and formed larger particles. While many of the nanoparticles are ∼5−10 nm in size, there are a few that are ∼50 nm assemblies that are composed of substructures of ∼5 to 10 nm.

Figure 3c shows one of the ∼5 × 10 nm nanoparticles where the Ir lattice spacing has increased as indicated by white lines in the image (inset), resulting in what appears to be an outer shell. From HRTEM imaging (Figure 3d), the shell has a lattice spacing of ∼0.41 nm, which matches with that of a Ir_3Li lattice (see Figure S12 and Figure S13). The electron diffraction pattern in Figure 3c (inset) also confirms that the shell is Ir_3Li as it shows an additional diffraction ring with dots corresponding to the double lattice spacing of Ir_3Li as marked by green arrows. Under the electron beam of intensity of 80 kV, the Ir_3Li shell structure disappears within a few minutes as Li atoms leave and the lattice spacing within the shell shrinks by ∼50% to ∼0.22 nm (back to that of Ir) and the additional electron diffraction ring disappears further confirming the Ir_3Li intermetallic presence in the nanoparticles (see Figure S14). Further, a thin layer (∼1−2 nm thick) is observed on the outside surface of the core−shell nanoparticle, as shown in Figure 3c. On the basis of DEMS, micro-Raman, and titration, this is presumably due to the LiO_2 discharge product that grows as a thin film, although we were unable to determine its lattice spacing due to lack of resolution.

The larger assemblies of about ∼50 nm are composed of substructures (see Figure S15). In these assemblies the Li atoms have also intercalated into the Ir surface region, forming an Ir−Li ordered structure showing up as white lines. These results confirm the presence of an Ir_3Li intermetallic in the Ir nanoparticles. Thus, during discharge the Ir nanoparticles of ∼1.5 nm in size agglomerate and form approximate core−shell Ir/Ir_3Li nanoparticles of ∼5 to 10 nm in size, some of which form larger assemblies. We note that some of the Li may also have penetrated into the core part.

We also investigated the evolution of the Ir nanoparticles during discharge and their stability after charge. The evolution was examined by stopping the cell after a capacity of ∼300 mAh/g was reached during discharge. The TEM results for the cathode shown in Figure 3e indicate that the interparticle distances are not uniform. Rather at places the particles are getting closer to each other and at other points there are empty patches. This indicates an onset of aggregation. The TEM image shown in the inset of Figure 3e captures where two have merged but have not yet coalesced completely. It was difficult to detect whether Li intercalation in these small particles has started due to the early stage of discharge. We also examined the cathode after charge (discharge of 1000 mAh/g and charge of 1000 mAh/g) to determine whether the Ir_3Li particles were stable. We found that the Ir_3Li nanoparticles remained after charge with a similar size. One such Ir_3Li nanoparticle is shown in Figure 3f (the presence of intercalated Li on the Ir nanoparticle is confirmed from electron energy loss spectroscopy (EELS) measurement and is shown in Figure S16. A Raman spectrum taken on the charged cathode surface also showed no evidence of the presence of LiO_2 as shown in

DOI: 10.1021/acs.jpca.9b06875
J. Phys. Chem. A 2019, 123, 10047−10056

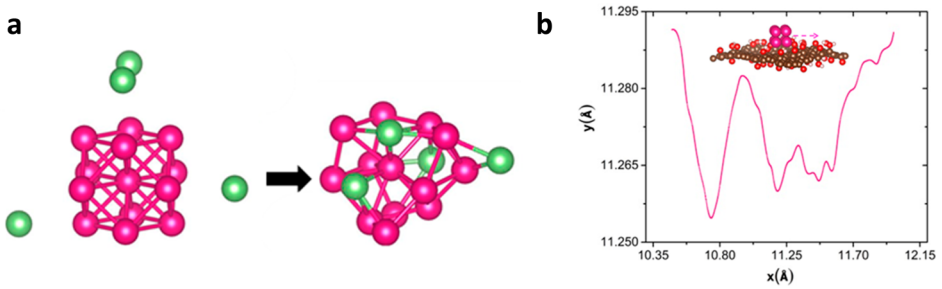

Figure 4. AIMD simulations. (a) AIMD simulation showing Li insertion into an Ir cluster (left) with an energy lowering of about 0.2 eV. This is used to estimate possible heating from Li intercalation. Note that LiO_2 is assumed to be the source of the Li, but the O_2 is not included in this simplified model. (b) Plot of *x*, *y* coordination of center of mass of Ir cluster on rGO surface (shown in figure) at 2000 K for ∼2 ps showing anomalous diffusion.

Figure S17, which further confirms that the Li is from the Ir_3Li nanoparticle). Thus, there is evidence that the Ir_3Li nanoparticles remain stable after charge.

4. DISCUSSION OF THE DISCHARGE MECHANISM

In this section we discuss a possible discharge mechanism based on the results described in section 3, along with some additional experiments and simulations. The experimental results obtained so far indicate the following. First, the HRTEM results prove conclusively that the Li is incorporated as Ir_3Li into the outer region of the Ir nanoparticles during discharge. Second, the nanoparticles evolve in size during discharge from ∼1.5 nm in size to larger nanoparticles of about 5−10 nm in size, with some clusters of nanoparticles as large as 50 nm. The HRTEM results indicate that the 5−10 nm nanoparticles are core−shell in nature with an Ir_3Li shell and an Ir core. Finally a thin layer (∼1−2 nm thick) is observed on the outside surface of the core−shell nanoparticle that is probably the LiO_2 discharge product.

The mechanism by which the Li is inserted into Ir to form the Ir_3Li intermetallic was investigated to determine whether oxygen is required for the formation of the intermetallic. This was done by carrying out the discharge with Ar instead of O_2. When Ar is used (with a discharge potential cutoff of 2 V), essentially no discharge occurs at 2.7 V and it stops very quickly (see Figure S18). This means that O_2 is required during discharge for the lithiation of Ir, and Li cations do not by themselves intercalate into the Ir nanoparticles. According to DFT calculations the reaction

$$LiO_2(s) + 3Ir(s) \rightarrow Ir_3Li(s) + O_2(g) \quad (1)$$

is very exothermic (−5.9 eV; see Table S1), suggesting that electrochemically formed LiO_2 during discharge provides the source of Li for formation of Ir_3Li, i.e., via reaction of the Ir with LiO_2. The TEM results (Figure 3f and Figure 3c) showing core−shell nanoparticles with Ir_3Li in the shell are consistent with this proposed mechanism whereby the Li is coming from a surface reaction Ir(s) with LiO_2 resulting in Li insertion near the surface. We have also examined the nanoparticles after charge by HRTEM and found that they remain lithiated with the Ir_3Li structure as shown in Figure 3f, indicating that Ir_3Li is very stable once formed, consistent with the reaction being very exothermic. We note that the only previous synthesis of an Ir_3Li intermetallic has been by high temperature synthesis using a temperature of 800 °C for 7 days.[12] These results suggest that a low temperature synthesis method based on electrochemical reactions is a new and previously unknown pathway.

We have carried out density functional (DFT) calculations to investigate how to account for the larger 5−10 nm nanoparticles observed with discharge. While the sintering of Ir_8 clusters to ∼1.5 nm clusters under annealing at 100 °C is understandable, the further increase to 5−10 nm nanoparticles at room temperature during discharge is puzzling. We have not found evidence for this in our previous study of Ag clusters used in Li−O_2 batteries.[11] In addition, careful X-ray investigations did not reveal any increase in size of supported Pd clusters (n = 4, 6, 17) after electrochemical cycling for water oxidation at room temperature.[27] We also note that this sintering is different from agglomeration occurring due to high coverage effects. The HRTEM images for the unannealed Ir_8 clusters on rGO in Figure 4 show evidence of agglomeration (mean size of 0.91 nm) at higher coverage (23% ML), but little at the lower coverage (13% ML). It has been previously noted that low coverage of supported small clusters is needed to prevent their agglomeration even at room temperature on other substrates.[11]

The DFT calculations were used to explore whether the localized heat generated by the reaction of Li with Ir, which is thermodynamically very favorable (see above), could cause the diffusion of Ir nanoparticles necessary to form larger nanoparticles. Calculations on model systems were used since the increase in size of the Ir nanoparticles takes place on a time scale too long for first-principles calculations and involves large particles. We first determined the approximate heat that would be generated by lithiation of Ir by carrying out AIMD simulations of Li reaction with a Ir_{13} cluster, as shown in Figure 4a. The results indicated a reaction energy of ∼0.2 eV or ∼2000 K. As a model system for studying diffusion of Ir and Ir_3Li particles, we have used Ir_8 clusters on an rGO surface in AIMD simulations at 2000 K. On the time scale of several picoseconds, the clusters are found to move around on the rGO surface, as shown in Figure 4b. The mean square displacement as a function of time shows deviation from linear behavior (Brownian motion), which is consistent with anomalous diffusion, as has been found experimentally recently for other small clusters.[28] At 300 K the particles on the surface are much less mobile (Figure S19). Thus, AIMD calculations suggest that the heat generated by lithiation could result in diffusion and sintering of the nanoparticles during discharge as observed in the experiments. In addition, since Li probably gets incorporated into the surface of the nanoparticles at the same time as the particles coalesce, there must also be Li segregation to the nanoparticle surface occurring.

DOI: 10.1021/acs.jpca.9b06875
J. Phys. Chem. A 2019, 123, 10047−10056

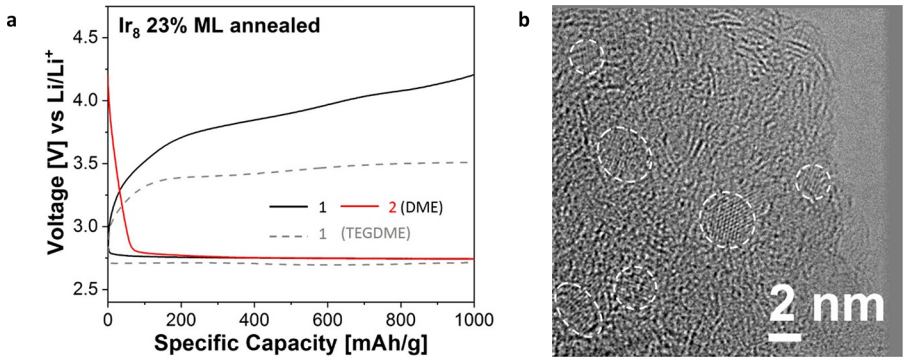

Figure 5. Voltage profile and TEM image of annealed Ir_8 clusters on rGO cycled in 1 M $LiCF_3SO_3$ in DME electrolyte. (a) Voltage profile for annealed 23% ML Ir_8–rGO cathode cycled in 1 M $LiCF_3SO_3$ in DME electrolyte (bold lines), overlaid with the same electrode cycled in 1 M $LiCF_3SO_3$ in TEGDME electrolyte (dashed lines). (b) TEM image of Ir nanoparticles on cathode surface imaged after first two discharge cycles showing a smaller size than for TEGDME. The particles range from ~1.5 to 3 nm.

The question of whether LiO_2 is responsible for Ir_3Li formation was further explored by using an electrolyte, dimethoxyethane (DME), which our results show does not favor LiO_2 formation in contrast to when TEGDME is used for the electrolyte. The Li–O_2 cell with DME was tested under identical conditions as for TEGDME with annealed Ir_8 clusters (23% ML) on the cathode surface. The cell was discharged to 1000 mAh/g using 1 M $LiCF_3SO_3$ in dimethyl ether (DME) as the electrolyte and then was charged. The voltage profile is shown in Figure 5a for this first cycle. The cell discharged at ~2.7 V similar to the results for TEGDME but charged at ~4.1 V significantly higher than what was found for TEGDME. These differing charge potentials suggest that the discharge product with DME is different from the LiO_2 formed with TEGDME. This was confirmed when the Ti(IV)OSO_4 based titration technique was used on the DME discharge product. A strong UV peak was obtained in the UV–vis spectra, which showed a Li_2O_2 content of 42%. Also we used HRTEM to investigate whether the Ir nanoparticles agglomerated as in the case of TEGDME and found that the nanoparticles were not nearly as large as shown in Figure 5b with no evidence for Ir_3Li. This result is consistent with the lack of LiO_2 formation in the case of DME. A possible explanation for this is that the ionic conductivity in DME is about 2 orders of magnitude larger than in TEGDME.[29−32] The faster diffusion of Li^+ or LiO_2 in DME may enhance formation of LiO_2 dimers for disproportionation in solution, accounting for the preference for Li_2O_2 formation in DME as opposed to TEGDME.

Finally, we consider the reason for the lower charge potential of the Li–O_2 battery with LiO_2 as a discharge product. The charge potential can depend on a number of factors including the composition of the discharge product (e.g., LiO_2 or Li_2O_2), morphology of the discharge product, its solubility in an aprotic electrolyte, electronic conductivity, and the oxygen evolution reaction effectiveness of the catalyst. In the case of the 23% ML coverage with annealed Ir_8 clusters, the charge potential was low (~3.4 V) for the first several cycles, as shown in Figure 1d. The low overpotential probably results from the good electronic conductivity of LiO_2 predicted from DFT calculations[9] in contrast to Li_2O_2, which usually has poor electronic conductivity. The subsequent increase in charge potential with cycling may be due to the deactivation or change in the Ir nanoparticles that are responsible for the templating mechanism for formation of LiO_2. If the Ir nanoparticles change such that they no longer act as a good template, this would result in formation of increasing amounts of Li_2O_2 with poor electronic conductivity and higher charge potential. This may also be responsible for the increase in charge potential seen for the other cases in Figure 1 (13 and 23% unannealed Ir_8 clusters) as well. Other factors could also be involved in the eventual failure of the cells after various numbers of cycles in Figure 1 such as side reactions involving the superoxide anion and singlet oxygen, electrolyte decomposition, Li anode corrosion, etc.[33−35]

Thus, the results from experiment and theory suggest a discharge mechanism depicted in the schematic in Figure 6. It

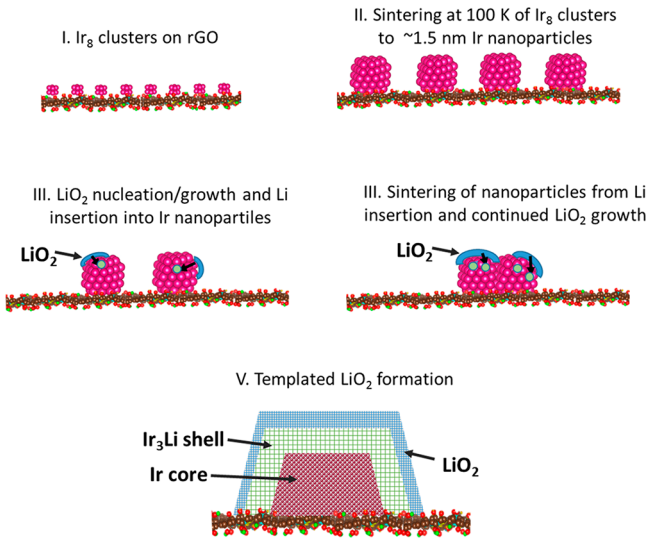

Figure 6. Schematic of evolution of Ir clusters to core–shell Ir/Ir_3Li nanoparticles. (I and II refer to prior to use in the Li-O_2 cell and III-V refer to in Li-O_2 cell.)

involves a synergistic process of both lithium intercalation of Ir to form nanoparticles with Ir_3Li outer regions and sintering from local heating of the nanoparticles into larger ones. The Ir_3Li intermetallic provides for stabilization of the LiO_2 by the lattice match between Ir_3Li and LiO_2.[9] The *in situ* Ir_3Li formation provides for an active cathode material that supports the LiO_2 formation and as a result a lower charge potential of the Li–O_2 battery.

DOI: 10.1021/acs.jpca.9b06875
J. Phys. Chem. A 2019, 123, 10047−10056

5. CONCLUSIONS

The following conclusions can be drawn from this investigation of cathodes for Li−O_2 batteries based on size-specific Ir clusters (n = 2, 4, 8) deposited on an rGO support:

(1) The performance of a Li−O_2 battery based on the clusters was found to depend on whether they were annealed to larger nanoparticles. Low charge potentials were found for the Ir_8 clusters annealed to form ∼1.5 nm nanoparticles, while higher charge potentials were found for clusters that were not annealed.

(2) The nanoparticles were found to evolve in size during first discharge from ∼1.5 nm in size to larger nanoparticles of about 5−10 nm in size, with some aggregates as large as 50 nm. They also remain that size after the first charge.

(3) On the basis of HRTEM results, the Li becomes incorporated into the outer region of the Ir nanoparticles to form *in situ* an Ir_3Li intermetallic giving nanoparticles with Ir_3Li shell and a Ir core. The only previous synthesis of an Ir_3Li intermetallic has been by high temperature synthesis, and these new results suggest that there is a low temperature synthesis method for Ir_3Li based on an electrochemical reaction involving LiO_2.

(4) On the basis of DEMS, Raman, and titration evidence, the discharge product is LiO_2, the growth of which can be attributed to the Ir_3Li acting as a template for its stabilization due to its good lattice match. In addition, the LiO_2 discharge product enables the observed low charge potential because of it is electronic conductivity.

Thus, this study has revealed the *in situ* formation of Ir_3Li nanoparticles in a Li−O_2 battery that can act as templates to promote formation of lithium superoxide in the cell. Other intermetallics such as Al−Li and In−Li have lattice matches with LiO_2 and could also serve as templates for LiO_2 growth. The core−shell nanoparticles provide a new direction in cathode material research for reducing charge overpotentials in Li−O_2 batteries.

■ ASSOCIATED CONTENT

Supporting Information

The Supporting Information is available free of charge on the ACS Publications website at DOI: 10.1021/acs.jpca.9b06875.

Schematic of the cluster deposition setup, mass spectrum, voltage profiles of Ir_2 and Ir_4 based cathodes, HAADF and TEM images, DOS, SEM images, DEMS calibration, Raman spectra of discharged and aged cathodes, titration, EDS spectra, and TEM results for discharged cathodes, crystal structure of Ir_3Li, HRTEM images and lattice spacing, EELS and Raman spectrum of charged cathodes, discharge voltage profile using Ar in the cell in place of O_2, AIMD simulations of Ir clusters, and table of formation energies for thermodynamics of Li insertion into Ir (PDF)

■ AUTHOR INFORMATION

Corresponding Authors

*Štefan Vajda (stefan.vajda@jh-inst.cas.cz).
*Khalil Amine (amine@anl.gov).
*Larry Curtiss (curtiss@anl.gov).

ORCID

J. G. Wen: 0000-0002-3755-0044
Pedram Abbasi: 0000-0001-6835-3062
Jun Lu: 0000-0003-0858-8577
Kah Chun Lau: 0000-0002-4925-3397
Rajeev S. Assary: 0000-0002-9571-3307
Yun Jung Lee: 0000-0003-3091-1174
Stefan Vajda: 0000-0002-1879-2099
Khalil Amine: 0000-0001-9206-3719
Larry A. Curtiss: 0000-0001-8855-8006

Notes

The authors declare no competing financial interest.

■ ACKNOWLEDGMENTS

The work of L.A.C., K.A., J.L., H.W., A.T.N., and X.L. was supported by the U.S. Department of Energy under Contract DE-AC02-06CH11357 from the Vehicle Technologies Office, Office of Energy Efficiency and Renewable Energy. The work of S.V. and A.H. was supported by the U.S. Department of Energy under Contract DE-AC02-06CH11357 from the Office of Science, Basic Energy Sciences, Division of Materials Science and Engineering. The work of K.C.L and R.S.A. was supported by the U.S. Department of Energy under Contract DE-AC02-06CH11357 from the Joint Center for Energy Storage Research (JCESR), an Energy Innovation Hub funded by the Office of Science, Basic Energy Sciences. P.A., M.A., and A.S. acknowledge support from the University of Illinois-Chicago Chancellor Proof of Concept Fund. S.V. also acknowledges support from the European Union's Horizon 2020 Research and Innovation Program under grant agreement No 810310, which corresponds to the J. Heyrovsky Chair project ("ERA Chair at J. Heyrovský Institute of Physical Chemistry AS CR − The institutional approach towards ERA") during the finalization of the paper. The funders had no role in the preparation of the article. Use of the Center for Nanoscale Materials, an Office of Science user facility, was supported by the U.S. Department of Energy, Office of Science, Basic Energy Sciences, under Contract No. DE-AC02-06CH11357. Use of the Advanced Photon Source, of Argonne National Laboratory an Office of Science user facility (beamline 13-BM), was supported by the U.S. Department of Energy, Office of Science, Basic Energy Sciences, under Contract No. DE-AC02-06CH11357.We acknowledge grants of computer time on the ALCF Bebop Cluster at Argonne National Laboratory. We acknowledge help with synthesis from Young Joo Lee, Do Hyung Kim, Tae-Geun Kang. S.V., L.A.C., J.L., and K.A. designed the experiments; A.H., S.V., Y.J.L., H.W., and C.Z. synthesized the cathodes; A.H. and S.V synthesized and deposited clusters; J.G.W., A.H., X.L., and D.M. performed and analyzed the TEM imaging experiments; X.L., D.Z., and J.L. performed and analyzed the X-ray measurements; J.L., X.L., A.H., R.A., C.Z., and H.W. tested the cathode materials; P.A., M.A., and A.S performed the DEMS measurements, H.W. and C.Z. performed the Raman and titration experiments, A.T.N., K.C.L., P.C.R., R.S.A., and L.A.C. were responsible for the theoretical computations. L.A.C., S.V., and K.A. supervised the project; A.H., L.A.C., S.V., and K.A. wrote the paper. All of the authors discussed the results and reviewed the manuscript.

■ REFERENCES

(1) Grande, L.; Paillard, E.; Hassoun, J.; Park, J.-B.; Lee, Y.-J.; Sun, Y.-K.; Passerini, S.; Scrosati, B. The Lithium/Air Battery: Still an

DOI: 10.1021/acs.jpca.9b06875
J. Phys. Chem. A 2019, 123, 10047−10056

Emerging System or a Practical Reality? *Adv. Mater.* **2015**, *27*, 784−800.
(2) Lu, J.; Lau, K. C.; Sun, Y. K.; Curtiss, L. A.; Amine, K. Review-Understanding and Mitigating Some of the Key Factors that Limit Non-Aqueous Lithium-Air Battery Performance. *J. Electrochem. Soc.* **2015**, *162*, A2439−A2446.
(3) Bruce, P. G.; Freunberger, S. A.; Hardwick, L. J.; Tarascon, J. M. Li-O_2 and Li-S batteries with High Energy Storage. *Nat. Mater.* **2012**, *11*, 19−29.
(4) Lu, J.; Chen, Z. H.; Ma, Z. F.; Pan, F.; Curtiss, L. A.; Amine, K. The Role of Nanotechnology in the Development of Battery Materials for Electric Vehicles. *Nat. Nanotechnol.* **2016**, *11*, 1031−1038.
(5) Aurbach, D.; McCloskey, B. D.; Nazar, L. F.; Bruce, P. G. Advances in Understanding Mechanisms Underpinning Lithium−Air Batteries. *Nat. Energy* **2016**, *1*, 16128.
(6) Zhai, D. Y.; Wang, H. H.; Yang, J. B.; Lau, K. C.; Li, K. X.; Amine, K.; Curtiss, L. A. Disproportionation in Li-O_2 Batteries Based on a Large Surface Area Carbon Cathode. *J. Am. Chem. Soc.* **2013**, *135*, 15364−15372.
(7) Gittleson, F. S.; Yao, K. P. C.; Kwabi, D. G.; Sayed, S. Y.; Ryu, W. H.; Shao-Horn, Y.; Taylor, A. D. Raman Spectroscopy in Lithium-Oxygen Battery Systems. *ChemElectroChem* **2015**, *2*, 1446−1457.
(8) Olivares-Marín, M.; Sorrentino, A.; Lee, R.-C.; Pereiro, E.; Wu, N.-L.; Tonti, D. Spatial Distributions of Discharged Products of Lithium−Oxygen Batteries Revealed by Synchrotron X-ray Transmission Microscopy. *Nano Lett.* **2015**, *15*, 6932−6938.
(9) Lu, J.; Lee, Y. J.; Luo, X. Y.; Lau, K. C.; Asadi, M.; Wang, H. H.; Brombosz, S.; Wen, J. G.; Zhai, D. Y.; Chen, Z. H.; et al. A Lithium-Oxygen Battery Based on Lithium Superoxide. *Nature* **2016**, *529*, 377−382.
(10) Lau, K. C.; Assary, R. S.; Redfern, P.; Greeley, J.; Curtiss, L. A. Electronic Structure of Lithium Peroxide Clusters and Relevance to Lithium-Air Batteries. *J. Phys. Chem. C* **2012**, *116*, 23890−23896.
(11) Lu, J.; Cheng, L.; Lau, K. C.; Tyo, E.; Luo, X.; Wen, J.; Miller, D.; Assary, R. S.; Wang, H. H.; Redfern, P.; et al. Effect of the Size-Selective Silver Clusters on Lithium Peroxide Morphology in Lithium-Oxygen Batteries. *Nat. Commun.* **2014**, *5*, 4895.
(12) Donkersloot, H. C.; Vanvucht, J. H. N. The Crystal Structure of IrLi, Ir_3Li and $LiRh_3$. *J. Less-Common Met.* **1976**, *50*, 279−282.
(13) Xu, Y.; Sheng, K.; Li, C.; Shi, G. Self-Assembled Graphene Hydrogel Via a One-Step Hydrothermal Process. *ACS Nano* **2010**, *4*, 4324−4330.
(14) Hummers, W. S.; Offeman, R. E. Preparation of Graphitic Oxide. *J. Am. Chem. Soc.* **1958**, *80*, 1339−1339a.
(15) Yin, C.; Tyo, E.; Kuchta, K.; Issendorff, B. v.; Vajda, S. Atomically Precise (Catalytic) Particles Synthesized by a Novel Cluster Deposition Instrument. *J. Chem. Phys.* **2014**, *140*, 174201.
(16) Luo, X.; Wu, T.; Lu, J.; Amine, K. Protocol of Electrochemical Test and Characterization of Aprotic Li-O2 Battery. *J. Visualized Exp.* **2016**, *113*, No. e53740.
(17) Kresse, G.; Furthmüller, J. Efficiency of Ab-Initio Total Energy Calculations for Metals and Semiconductors Using a Plane-Wave Basis Set. *Comput. Mater. Sci.* **1996**, *6*, 15−50.
(18) Kresse, G.; Joubert, D. From Ultrasoft Pseudopotentials to the Projector Augmented-Wave Method. *Phys. Rev. B: Condens. Matter Mater. Phys.* **1999**, *59*, 1758−1775.
(19) Perdew, J. P.; Burke, K.; Ernzerhof, M. Generalized Gradient Approximation Made Simple. *Phys. Rev. Lett.* **1996**, *77*, 3865−3868.
(20) Zhai, D.; Lau, K. C.; Wang, H.-H.; Wen, J.; Miller, D. J.; Lu, J.; Kang, F.; Li, B.; Yang, W.; Gao, J.; et al. Interfacial Effects on Lithium Superoxide Disproportionation in Li-O_2 Batteries. *Nano Lett.* **2015**, *15*, 1041−1046.
(21) Sutton, L. E. *Tables of Interatomic Distances and Configuration in Molecules and Ions: Supplement 1956−59*; Chemical Society, 1965.
(22) Zhai, D. Y.; Wang, H. H.; Lau, K. C.; Gao, J.; Redfern, P. C.; Kang, F. Y.; Li, B. H.; Indacochea, E.; Das, U.; Sun, H. H.; et al. Raman Evidence for Late Stage Disproportionation in a Li-O-2 Battery. *J. Phys. Chem. Lett.* **2014**, *5*, 2705−2710.
(23) Zhai, D. Y.; Lau, K. C.; Wang, H. H.; Wen, J. G.; Miller, D. J.; Kang, F. Y.; Li, B. H.; Zavadil, K.; Curtiss, L. A. The Effect of Potassium Impurities Deliberately Introduced into Activated Carbon Cathodes on the Performance of Lithium-Oxygen Batteries. *ChemSusChem* **2015**, *8*, 4235−4241.
(24) Papp, J. K.; Forster, J. D.; Burke, C. M.; Kim, H. W.; Luntz, A. C.; Shelby, R. M.; Urban, J. J.; McCloskey, B. D. Poly(vinylidene fluoride) (PVDF) Binder Degradation in Li−O2 Batteries: A Consideration for the Characterization of Lithium Superoxide. *J. Phys. Chem. Lett.* **2017**, *8*, 1169−1174.
(25) Halder, A.; Wang, H. H.; Lau, K. C.; Assary, R. S.; Lu, J.; Vajda, S.; Amine, K.; Curtiss, L. A. Identification and Implications of Lithium Superoxide in Li-O-2 Batteries. *Acs Energy Lett.* **2018**, *3*, 1105−1109.
(26) Wang, H. H.; Lee, Y. J.; Assary, R. S.; Zhang, C. J.; Luo, X. Y.; Redfern, P. C.; Lu, J.; Lee, Y. J.; Kim, D. H.; Kang.; et al. Lithium Superoxide Hydrolysis and Relevance to Li-O-2 Batteries. *J. Phys. Chem. C* **2017**, *121*, 9657−9661.
(27) Kwon, G.; Ferguson, G. A.; Heard, C. J.; Tyo, E. C.; Yin, C. R.; DeBartolo, J.; Seifert, S.; Winans, R. E.; Kropf, A. J.; Greeley, J.; et al. Size-Dependent Subnanometer Pd Cluster (Pd_4, Pd_6, and Pd_{17}) Water Oxidation Electrocatalysis. *ACS Nano* **2013**, *7*, 5808−5817.
(28) Furnival, T.; Leary, R. K.; Tyo, E. C.; Vajda, S.; Ramasse, Q. M.; Thomas, J. M.; Bristowe, P. D.; Midgley, P. A. Anomalous Diffusion of Single Metal Atoms on a Graphene Oxide Support. *Chem. Phys. Lett.* **2017**, *683*, 370−374.
(29) Hayamizu, K.; Aihara, Y. Ion and Solvent Diffusion and Ion Conduction of PC-DEC and PC-DME Binary Solvent Electrolytes of $LiN(SO_2CF_3)_2$. *Electrochim. Acta* **2004**, *49*, 3397−3402.
(30) D'Angelo, A. J.; Panzer, M. J. Enhanced Lithium Ion Transport in Poly(ethylene glycol) Diacrylate-Supported Solvate Ionogel Electrolytes via Chemically Cross-linked Ethylene Oxide Pathways. *J. Phys. Chem. B* **2017**, *121*, 890−895.
(31) Gittleson, F. S.; Jones, R. E.; Ward, D. K.; Foster, M. E. Oxygen Solubility and Transport in Li-Air Battery Electrolytes: Establishing Criteria and Strategies for Electrolyte Design. *Energy Environ. Sci.* **2017**, *10*, 1167−1179.
(32) Yoshida, K.; Tsuchiya, M.; Tachikawa, N.; Dokko, K.; Watanabe, M. Change from Glyme Solutions to Quasi-ionic Liquids for Binary Mixtures Consisting of Lithium Bis-(trifluoromethanesulfonyl)amide and Glymes. *J. Phys. Chem. C* **2011**, *115*, 18384−18394.
(33) Mourad, E.; Petit, Y. K.; Spezia, R.; Samojlov, A.; Summa, F. F.; Prehal, C.; Leypold, C.; Mahne, N.; Slugovc, C.; Fontaine, O.; et al. Singlet Oxygen from Cation Driven Superoxide Disproportionation and Consequences for Aprotic Metal−O_2 Batteries. *Energy Environ. Sci.* **2019**, *12*, 2559−2568.
(34) Mahne, N.; Schafzahl, B.; Leypold, C.; Leypold, M.; Grumm, S.; Leitgeb, A.; Strohmeier, G. A.; Wilkening, M.; Fontaine, O.; Kramer, D.; et al. Singlet Oxygen Generation as a Major Cause for Parasitic Reactions during Cycling of Aprotic Lithium−Oxygen Batteries. *Nat. Energy* **2017**, *2*, 17036.
(35) Assary, R. S.; Lu, J.; Du, P.; Luo, X. Y.; Zhang, X. Y.; Ren, Y.; Curtiss, L. A.; Amine, K. The Effect of Oxygen Crossover on the Anode of a Li-O2 Battery using an Ether-Based Solvent: Insights from Experimental and Computational Studies. *ChemSusChem* **2013**, *6*, 51−55.

DOI: 10.1021/acs.jpca.9b06875
J. Phys. Chem. A 2019, 123, 10047−10056